

Active-sterile Neutrino Oscillations in Neutrino-driven Winds: Implications for Nucleosynthesis

ZEWI XIONG,¹ MENG-RU WU,^{2,3} AND YONG-ZHONG QIAN^{1,4}

¹*School of Physics and Astronomy, University of Minnesota, Minneapolis, Minnesota 55455, USA*

²*Institute of Physics, Academia Sinica, Taipei 11529, Taiwan*

³*Institute of Astronomy and Astrophysics, Academia Sinica, Taipei 10617, Taiwan*

⁴*Tsung-Dao Lee Institute, Shanghai 200240, People's Republic of China*

(Received; Revised; Accepted)

ABSTRACT

A protoneutron star produced in a core-collapse supernova (CCSN) drives a wind by its intense neutrino emission. We implement active-sterile neutrino oscillations in a steady-state model of this neutrino-driven wind to study their effects on the dynamics and nucleosynthesis of the wind in a self-consistent manner. Using vacuum mixing parameters indicated by some experiments for a sterile ν_s of ~ 1 eV in mass, we observe interesting features of oscillations due to various feedback. For the higher ν_s mass values, we find that oscillations can reduce the mass loss rate and the wind velocity by a factor of ~ 1.6 – 2.7 and change the electron fraction critical to nucleosynthesis by a significant to large amount. In the most dramatic cases, oscillations shifts nucleosynthesis from dominant production of ^{45}Sc to that of ^{86}Kr and ^{90}Zr during the early epochs of the CCSN evolution.

Keywords: neutrinos — nuclear reactions, nucleosynthesis, abundances — stars: mass-loss — stars: neutron — supernovae: general

1. INTRODUCTION

In this paper we study the effects of active-sterile neutrino oscillations on the dynamics and nucleosynthesis of neutrino-driven winds. The proto-neutron star (PNS) formed in a core-collapse supernova (CCSN) is a profuse source of ν_e , $\bar{\nu}_e$, ν_μ , $\bar{\nu}_\mu$, ν_τ , and $\bar{\nu}_\tau$. These neutrinos interact with the material in the vicinity of the PNS mainly through

$$\nu_e + n \rightarrow p + e^-, \quad (1a)$$

$$\bar{\nu}_e + p \rightarrow n + e^+. \quad (1b)$$

This heating drives a wind (Duncan et al. 1986), which eventually becomes part of the ejecta from the CCSN. This neutrino-driven wind has been studied extensively as a site for production of elements heavier than the Fe group (Woosley & Baron 1992; Woosley & Hoffman 1992; Meyer et al. 1992; Woosley et al. 1994; Wittl et al. 1994; Takahashi et al. 1994; Qian & Woosley 1996; Hoffman et al. 1997; Wanajo et al. 2001; Thompson et al. 2001; Roberts et al. 2010; Wanajo 2013). The neutrino reactions in Eqs. (1a) and (1b) not only provide the heating, but also determine the neutron-to-proton ratio of the wind (Qian et al. 1993; Qian & Woosley 1996). This ratio is equivalent to the net number of electrons per baryon, i.e., the electron fraction Y_e , and is a critical parameter for nucleosynthesis. Because neutrinos of different flavors interact differently with matter, neutrino flavor oscillations would potentially impact the dynamics and nucleosynthesis of the wind (e.g., Qian et al. 1993). Here we focus on the oscillations between ν_e ($\bar{\nu}_e$) and ν_s ($\bar{\nu}_s$), where ν_s ($\bar{\nu}_s$) is a sterile species that does not have normal weak interaction like an active one.

The existence of sterile neutrinos have been discussed based on both theoretical and experimental considerations (e.g., Abazajian et al. 2012). Potential effects of active-sterile neutrino oscillations on the dynamics and nucleosynthesis of CCSNe have also been studied (e.g., Nunokawa et al. 1997; McLaughlin et al. 1999; Tamborra et al. 2012; Wu et al. 2014; Pllumbi et al. 2015). These previous studies, however, are not fully self-consistent in that they did not take into account the feedback of active-sterile neutrino oscillations on the velocity (v), density (ρ), and temperature (T) profiles of the CCSN. In this paper we make a significant step towards treating such feedback by coupling neutrino flavor evolution with the evolution of v , ρ , T , and Y_e in the neutrino-driven wind.

This paper is organized as follows. In §2, we describe our steady-state model of the neutrino-driven wind including active-sterile neutrino oscillations. In §3, we present the results for nine cases that correspond to winds ejected at three representative times of CCSN evolution with three different sets of neutrino oscillation parameters. For each case, we show the profiles of v , ρ , T , and Y_e in the wind and compare them with those in the absence of oscillations. In §4, we show the effects of active-sterile neutrino oscillations on nucleosynthesis in the wind. We summarize our results and give conclusions in §5.

2. MODEL OF THE NEUTRINO-DRIVEN WIND

A massive star arrives at the end of its life when nuclear fuel is exhausted in its core. The core undergoes gravitational collapse and bounces when supranuclear density is reached at the center and a PNS is born. The bounce launches a shock, which is stalled on the way out of the core due to energy loss from dissociating nuclei into mostly free nucleons. How this shock is revived to make an explosion is the crux of the CCSN mechanism (e.g., Janka 2012). Neutrinos emitted by the PNS are thought to play a critical role by heating the material behind the stalled shock mainly through the reactions in Eqs. (1a) and (1b) (Bethe & Wilson 1985). Because the neutrino emission lasts for ~ 10 s, the same heating continues to drive a mass outflow, the so-called neutrino-driven wind, after the shock is revived.

While the wind can be studied within a CCSN simulation, its physical conditions can be understood quite well by treating it as a stationary mass outflow between the PNS and the shock (Qian & Woosley 1996). In the latter approach, the wind is the solution to an eigenvalue problem with the inner and outer boundaries specified by the PNS and shock, respectively. The eigenvalue to be determined is the mass loss rate \dot{M} . We will take this approach in this paper. The inner boundary is specified by the radius R_ν of the PNS, which also defines the surface of neutrino emission, or the neutrinosphere. On the timescale for a mass element in the wind to receive significant neutrino heating, the neutrino luminosities and energy spectra at emission stay approximately fixed. Therefore, the wind can be considered as a steady-state configuration obtained for a PNS with a fixed R_ν and a fixed mass M_{PNS} that emits neutrinos with fixed luminosities and energy spectra.

2.1. Equations for the wind

In this paper we ignore the effects of general relativity. To good approximation, v is nonrelativistic and the internal energy of a mass element in the wind is much smaller than its rest-mass energy. Based on the above considerations, the equations describing a spherically-symmetric steady-state wind (e.g., Qian & Woosley 1996) are

$$4\pi r^2 \rho v = \dot{M}, \quad (2a)$$

$$v \frac{dv}{dr} = -\frac{1}{\rho} \frac{dP}{dr} - \frac{GM_{\text{PNS}}}{r^2}, \quad (2b)$$

$$\frac{d\epsilon}{dr} - \frac{P}{\rho^2} \frac{d\rho}{dr} = \frac{\dot{q}}{v}, \quad (2c)$$

$$\frac{dY_e}{dr} = \frac{1}{v} [(\lambda_{\nu_e n} + \lambda_{e+n})Y_n - (\lambda_{\bar{\nu}_e p} + \lambda_{e-p})Y_p], \quad (2d)$$

where P is the pressure, G is the gravitational constant, ϵ is the internal energy per unit mass, \dot{q} is the rate of net energy gain per unit mass, Y_n (Y_p) is the number of free neutrons (protons) per baryon, i.e., the number fraction of free neutrons (protons), and $\lambda_{\nu_e n}$ (λ_{e-p}) and $\lambda_{\bar{\nu}_e p}$ (λ_{e+n}) are the rates per target nucleon for the reactions (inverse reactions) in Eqs. (1a) and (1b), respectively.

The equation of state determines P and ϵ as functions of ρ , T , and the composition of the wind. We assume that the wind is electrically neutral and composed of neutrons, protons, α -particles, electrons, positrons, and photons. We further assume nuclear statistical equilibrium (NSE) to determine the number fractions of the nuclear components, Y_n , Y_p , and Y_α :

$$Y_n + Y_p + 4Y_\alpha = 1, \quad (3a)$$

$$Y_p + 2Y_\alpha = Y_e, \quad (3b)$$

$$Y_\alpha = \frac{1}{2} Y_n^2 Y_p^2 \left(\frac{\rho}{m_u} \right)^3 \left(\frac{2\pi}{m_u T} \right)^{9/2} \exp\left(\frac{B_\alpha}{T} \right), \quad (3c)$$

where m_u is the atomic mass unit and $B_\alpha \approx 28.3$ MeV is the nuclear binding energy of the α -particle. We use the equation of state from Timmes & Arnett (1999) and Timmes & Swesty (2000) with the above composition. Note that in Eq. (3c) and hereafter, the speed of light c , the Planck constant \hbar , and the Boltzmann constant k are set to unity.

Given the inner and outer boundary conditions at the PNS and the shock, respectively, the eigenvalue \dot{M} can be determined by solving the wind equations once the rates \dot{q} , $\lambda_{\nu_e n}$, $\lambda_{e^+ n}$, $\lambda_{\bar{\nu}_e p}$, and $\lambda_{e^- p}$ are specified. In practice, we solve for v , ρ , T , and Y_e as functions of the radius r . The corresponding Y_n , Y_p , and Y_α are specified by NSE and the corresponding P and ϵ are obtained from the equation of state.

2.2. Rates for energy gain or loss and neutron-proton interconversion

The rate of net energy gain per unit mass, \dot{q} , is

$$\begin{aligned} \dot{q} = & \dot{q}_\alpha + 2\dot{q}_{\nu_x N} + 2\dot{q}_{\bar{\nu}_x N} + 2\dot{q}_{\nu_x e^\pm} + 2\dot{q}_{\bar{\nu}_x e^\pm} + 2\dot{q}_{\nu_x \bar{\nu}_x} \\ & + \dot{q}_{\nu_e n} + \dot{q}_{\bar{\nu}_e p} + \dot{q}_{\nu_e N} + \dot{q}_{\bar{\nu}_e N} + \dot{q}_{\nu_e e^\pm} + \dot{q}_{\bar{\nu}_e e^\pm} + \dot{q}_{\nu_e \bar{\nu}_e} \\ & - \dot{q}_{e^+ n} - \dot{q}_{e^- p} - \dot{q}_{e^+ e^-}, \end{aligned} \quad (4)$$

where

$$\dot{q}_\alpha = v \left(\frac{dY_\alpha}{dr} \right) \frac{B_\alpha}{m_u} \quad (5)$$

corresponds to formation of α -particles, $\dot{q}_{\nu_x N}$ and $\dot{q}_{\nu_x e^\pm}$ to scattering of ν_x (ν_μ or ν_τ) on nucleons and e^\pm , respectively, $\dot{q}_{\nu_x \bar{\nu}_x}$ to $\nu_x \bar{\nu}_x$ annihilation into e^\pm , $\dot{q}_{\nu_e n}$ ($\dot{q}_{e^- p}$) and $\dot{q}_{\bar{\nu}_e p}$ ($\dot{q}_{e^+ n}$) to the reactions (inverse reactions) in Eqs. (1a) and (1b), respectively, and $\dot{q}_{e^+ e^-}$ to e^\pm annihilation into neutrinos and antineutrinos of all three active flavors. The rates denoted by other subscripts are similar to those mentioned above. The factor of two associated with ν_x ($\bar{\nu}_x$) assumes that ν_μ and ν_τ ($\bar{\nu}_\mu$ and $\bar{\nu}_\tau$) have identical emission characteristics.

Contributions to \dot{q} , as well as the rates $\lambda_{\nu_e n}$, $\lambda_{e^+ n}$, $\lambda_{\bar{\nu}_e p}$, and $\lambda_{e^- p}$, can be separated into those that are directly affected by active-sterile neutrino oscillations and those that are not. Those rates on the second line of Eq. (4), as well as $\lambda_{\nu_e n}$ and $\lambda_{\bar{\nu}_e p}$, belong to the former, while those on the first and last lines of Eq. (4), as well as $\lambda_{e^+ n}$ and $\lambda_{e^- p}$, belong to the latter. All of the rates are described in detail in Appendix A. Below we highlight those rates associated with neutrino interaction processes.

We assume that all neutrinos are emitted from a neutrinosphere of radius R_ν with Fermi-Dirac spectra of zero chemical potential. For a specific neutrino species ν_a , its normalized spectrum is

$$f_{\nu_a}(E) = \frac{1}{F_2(0)T_{\nu_a}^3} \frac{E^2}{\exp(E/T_{\nu_a}) + 1}, \quad (6)$$

where T_{ν_a} is the temperature parameter characteristic of ν_a emission. In the above equation, $F_2(0)$ refers to the Fermi-Dirac integral defined as

$$F_k(y) = \int_0^\infty \frac{x^k}{\exp(x-y) + 1} dx. \quad (7)$$

At the neutrinosphere, the differential number density of ν_a per unit energy interval per unit solid angle is

$$\left(\frac{d^2 n_{\nu_a}}{dE d\Omega} \right)_{R_\nu} = \frac{L_{\nu_a}}{4\pi^2 R_\nu^2 \langle E_{\nu_a} \rangle} f_{\nu_a}(E), \quad (8)$$

where L_{ν_a} and $\langle E_{\nu_a} \rangle = T_{\nu_a} F_3(0)/F_2(0)$ are the luminosity and average energy, respectively, of ν_a at emission.

All neutrinos essentially free-stream above the neutrinosphere, but a small fraction can still interact, mostly with nucleons, e^\pm , and each other. The angle θ between the neutrino's velocity and the radial direction at emission is related to the angle θ_r defined in the same way at radius r by

$$\sin \theta_r = \frac{R_\nu}{r} \sin \theta. \quad (9)$$

Consequently, for an interaction point at radius r , only those neutrinos within the solid angle defined by polar angles $0 \leq \theta_r \leq \theta_r^{\max}$ are relevant, where θ_r^{\max} corresponds to a neutrino emitted tangentially at the neutrinosphere ($\theta = \pi/2$) and satisfies

$$\sin \theta_r^{\max} = \frac{R_\nu}{r}. \quad (10)$$

Within this solid angle at radius r , the differential number density of ν_a in the absence of neutrino oscillations is

$$\left(\frac{d^2 n_{\nu_a}}{dE d\Omega}\right)_r = \left(\frac{d^2 n_{\nu_a}}{dE d\Omega}\right)_{R_\nu}. \quad (11)$$

In the presence of active-sterile neutrino oscillations, the differential number density of active ν_a at radius r is

$$\left(\frac{d^2 n_{\nu_a}}{dE d\Omega}\right)_r^{\text{osc}} = \left(\frac{d^2 n_{\nu_a}}{dE d\Omega}\right)_r P_{\nu_a}(E, r), \quad (12)$$

where $P_{\nu_a}(E, r)$ is the probability for a ν_a emitted with energy E to survive as a ν_a at radius r .

As an example, we give the expression of $\lambda_{\nu_e n}$ at radius r in the presence of active-sterile neutrino oscillations:

$$\lambda_{\nu_e n} = \int \left(\frac{d^2 n_{\nu_e}}{dE d\Omega}\right)_r^{\text{osc}} \sigma_{\nu_e n}(E) dE d\Omega_r \quad (13a)$$

$$= \frac{G_F^2 |V_{ud}|^2 (1 + 3g_A^2)}{2\pi^2} \frac{L_{\nu_e} D(r)}{R_\nu^2 \langle E_{\nu_e} \rangle} \int_0^\infty (E + \Delta)^2 \left(1 - \frac{W_{\nu_e} E}{m_N}\right) f_{\nu_e}(E) P_{\nu_e}(E, r) dE, \quad (13b)$$

where

$$\sigma_{\nu_e n}(E) = \frac{G_F^2 |V_{ud}|^2 (1 + 3g_A^2)}{\pi} (E + \Delta)^2 \left(1 - \frac{W_{\nu_e} E}{m_N}\right) \quad (14)$$

is the cross section for ν_e absorption on neutrons and

$$D(r) = \frac{1}{2\pi} \int d\Omega_r = \int_0^{\theta_r^{\text{max}}} \sin \theta_r d\theta_r = 1 - \sqrt{1 - \frac{R_\nu^2}{r^2}}. \quad (15)$$

In Eq. (14), $\Delta \equiv m_n - m_p$ is the neutron-proton mass difference, $m_N = (m_n + m_p)/2$ is the average nucleon mass, the term associated with

$$W_{\nu_e} = \frac{2[1 + 5g_A^2 - 2g_A(1 + f_2)]}{1 + 3g_A^2} \quad (16)$$

is the correction due to weak magnetism and nucleon recoil, and G_F , V_{ud} , g_A , and f_2 are the standard constants describing the weak interaction of concern.

2.3. Active-sterile neutrino oscillations

We only consider ν_e - ν_s and $\bar{\nu}_e$ - $\bar{\nu}_s$ oscillations in this paper. We assume that neutrinos emitted with energy E but from different points on the neutrinosphere have the same flavor evolution as those traveling on the radial trajectory. For a radially-propagating ν_e emitted with energy E , the evolution of its wave function

$$\psi_{\nu_e}(E, r) = \begin{pmatrix} a_{\nu_e}(E, r) \\ a_{\nu_s}(E, r) \end{pmatrix} \quad (17)$$

is governed by

$$i \frac{d}{dr} \psi_{\nu_e}(E, r) = \mathbf{H}_{\nu_e}(E, r) \psi_{\nu_e}(E, r), \quad (18)$$

where a_{ν_e} (a_{ν_s}) is the amplitude for being a ν_e (ν_s), and

$$\mathbf{H}_{\nu_e}(E, r) = \mathbf{H}_{\text{vac}}(E) + \mathbf{H}_{\text{mat}}(r) + \mathbf{H}_{\nu\nu}(r) \quad (19)$$

is the propagation Hamiltonian. The three contributions to this Hamiltonian are

$$\mathbf{H}_{\text{vac}}(E) = \frac{\delta m^2}{4E} \begin{pmatrix} -\cos 2\theta_V & \sin 2\theta_V \\ \sin 2\theta_V & \cos 2\theta_V \end{pmatrix}, \quad (20)$$

where δm^2 is the vacuum mass-squared difference and θ_V is the vacuum mixing angle,

$$\mathbf{H}_{\text{mat}}(r) = \frac{V_{\text{mat}}(r)}{2} \begin{pmatrix} 1 & 0 \\ 0 & -1 \end{pmatrix}, \quad (21)$$

where

$$V_{\text{mat}}(r) = \frac{\sqrt{2}G_F}{2m_u}\rho(r)[3Y_e(r) - 1] \quad (22)$$

corresponds to neutrino forward scattering on e^\pm , neutrons, and protons (Wolfenstein 1978; Mikheev & Smirnov 1985, see also, e.g., Sigl & Raffelt 1993), and

$$\mathbf{H}_{\nu\nu}(r) = \frac{V_\nu(r)}{2} \begin{pmatrix} 1 & 0 \\ 0 & -1 \end{pmatrix}, \quad (23)$$

where

$$V_\nu(r) = \frac{\sqrt{2}G_FD(r)^2}{2\pi R_\nu^2} \int \left[\frac{L_{\nu_e}}{\langle E_{\nu_e} \rangle} f_{\nu_e}(E') P_{\nu_e}(E', r) - \frac{L_{\bar{\nu}_e}}{\langle E_{\bar{\nu}_e} \rangle} f_{\bar{\nu}_e}(E') P_{\bar{\nu}_e}(E', r) \right] dE' \quad (24)$$

corresponds to neutrino forward scattering on other neutrinos (e.g., Fuller et al. 1987; Sigl & Raffelt 1993). In Eq. (24), $P_{\bar{\nu}_e}(E, r)$ is calculated from the amplitude $a_{\bar{\nu}_e}(E, r)$, which in turn is determined along with $a_{\bar{\nu}_s}(E, r)$ by the same flavor evolution equation as Eq. (18), except with the Hamiltonian $\mathbf{H}_{\bar{\nu}_e}(E, r) = \mathbf{H}_{\text{vac}}(E) - \mathbf{H}_{\text{mat}}(r) - \mathbf{H}_{\nu\nu}(r)$. Because we only consider ν_e - ν_s and $\bar{\nu}_e$ - $\bar{\nu}_s$ oscillations, there is no flavor evolution for ν_x or $\bar{\nu}_x$. We further assume that ν_x and $\bar{\nu}_x$ have the same emission characteristics so that their contributions to $\mathbf{H}_{\nu\nu}(r)$ cancel.

2.4. Parameters and procedures

A number of experiments indicate the existence of a ν_s ($\bar{\nu}_s$) that mixes with ν_e ($\bar{\nu}_e$) for a range of plausible vacuum mixing parameters. As our major goal is to include active-sterile neutrino oscillations in a self-consistent treatment of the wind and to demonstrate their effects, we follow Wu et al. (2014) and consider three sets of δm^2 and $\sin^2 2\theta_V$ that are listed in Table 1 and referred to as Cases A, B, and C, respectively. For comparison, the case without oscillations is referred to as Case D. We plan to survey a broad range of mixing parameters in a separate paper.

Table 1. Cases of active-sterile neutrino oscillations

	δm^2 (eV ²)	$\sin^2 2\theta_V$
A	1.75	0.10
B	1.0	0.06
C	0.4	0.04
D	no	oscillations

To solve the wind equations, we need to specify properties of the PNS, especially the characteristics of its neutrino emission, the inner boundary conditions at the neutrinosphere, and the outer boundary conditions at the CCSN shock. We use the spherical CCSN model of Martínez-Pinedo et al. (2014) as a guide and consider three snapshots at time post core bounce $t_{\text{pb}} = 1, 2, \text{ and } 5$ s, respectively. The PNS mass is taken to be fixed at $M_{\text{PNS}} = 1.282M_\odot$. The neutrinosphere radius R_ν for each snapshot is given in Table 2 along with the luminosities and average energies of ν_e , $\bar{\nu}_e$, and ν_x at emission. As noted above, the emission characteristics of $\bar{\nu}_x$ are taken to be identical to those of ν_x . We assume that the shock launched by the CCSN explosion is unaffected by active-sterile neutrino oscillations. For the epoch of interest, the region at $r \gtrsim 10^3$ km enclosed by the shock has approximately the same temperature, which slowly decreases as the shock moves outward. We take the temperature at $r = 10^3$ km $\equiv R_b$ as the effective outer boundary condition set up by the CCSN shock. The values of $T(R_b)$ are given in Table 2 along with the corresponding temperatures $T(R_\nu)$ at the neutrinosphere. In addition to $T(R_\nu)$, the other inner boundary conditions are values of $\rho(R_\nu)$ and $Y_e(R_\nu)$, which are determined by assuming $\dot{q} = 0$ and $dY_e/dr = 0$ at the neutrinosphere. Note that for the vacuum mixing parameters of interest, ν_e - ν_s and $\bar{\nu}_e$ - $\bar{\nu}_s$ oscillations can be ignored at the neutrinosphere and $\rho(R_\nu)$ and $Y_e(R_\nu)$ correspond to conditions in the absence of neutrino oscillations. Accordingly, we assume that neutrinos and antineutrinos are in their pure active flavor states at the neutrinosphere.

For a specific set of δm^2 and $\sin^2 2\theta_V$ and a specific set of boundary conditions, we use the following procedure to determine $v(r)$, $\rho(r)$, $T(r)$, and $Y_e(r)$ for the wind: (1) calculate $\rho(R_\nu)$ and $Y_e(R_\nu)$ for the corresponding $T(R_\nu)$ using $\dot{q}(R_\nu) = 0$ and $(dY_e/dr)_{R_\nu} = 0$, (2) pick an estimated value of \dot{M} and calculate $v(R_\nu)$, (3) starting from $r = R_\nu$,

Table 2. Parameters at the inner and outer boundaries. Neutrino luminosities are given in units of 10^{51} erg s^{-1} . Average neutrino energies and temperatures are given in units of MeV.

t_{pb} (s)	R_ν (km)	L_{ν_e}	$L_{\bar{\nu}_e}$	L_{ν_x}	$\langle E_{\nu_e} \rangle$	$\langle E_{\bar{\nu}_e} \rangle$	$\langle E_{\nu_x} \rangle$	$T(R_\nu)$	$T(R_b)$
1	22.25	2.95	3.68	3.83	8.80	12.49	12.34	2.79	0.17
2	18.07	1.67	2.01	2.58	8.43	11.90	11.70	2.68	0.14
5	14.50	0.82	0.83	1.42	7.79	10.17	10.47	2.47	0.09

integrate the wind equations along with the equations of ν_e and $\bar{\nu}_e$ flavor evolution up to $r = R_b$, (4) repeat steps 2 and 3 until the value of $T(R_b)$ given by the wind solution satisfies the outer boundary condition. The corresponding \dot{M} is the eigenvalue of the mass loss rate for the wind.

3. RESULTS ON NEUTRINO-DRIVEN WINDS

Below we present the results on the wind for three sets of vacuum mixing parameters (cases A, B, and C in Table 1) and for three snapshots of the CCSN evolution ($t_{\text{pb}} = 1, 2,$ and 5 s). We also compare these results with those in the absence of neutrino oscillations.

3.1. Mass loss rates and profiles of v , ρ , and T

The results on the wind mass loss rate \dot{M} for each case of interest are given in Table 3, and those on the profiles of v , ρ , and T are shown in Fig. 1. For all three snapshots, the wind solutions for the vacuum mixing parameters of case C are very close to those in the absence of neutrino oscillations (case D), whereas the solutions for case A show the largest deviations. The solutions for case B are similar to those for case A for $t_{\text{pb}} = 1$ s, but become similar to case C for $t_{\text{pb}} = 5$ s. In addition, the effects of oscillations on \dot{M} and the profile of v are much more significant than those on the profiles of ρ and T . As case A corresponds to the largest effects of oscillations, we focus on this case in this subsection.

Table 3. Mass loss rates in units of $M_\odot s^{-1}$. The letters refer to the sets of vacuum mixing parameters in Table 1 and $X(Y)$ denotes $X \times 10^Y$.

t_{pb} (s)	A	B	C	D
1	6.95(-5)	7.10(-5)	1.86(-4)	1.87(-4)
2	2.40(-5)	2.76(-5)	3.80(-5)	3.81(-5)
5	2.82(-6)	4.16(-6)	4.50(-6)	4.51(-6)

The rate of net energy gain per unit mass \dot{q} is crucial to the understanding of the wind. This quantity is shown as functions of r and T , respectively, in Figs. 2(a)-(f). Our inner boundary conditions require $\dot{q}(R_\nu) = 0$. Because the rate of cooling is sensitive to T , it decreases more rapidly than the rate of heating by neutrinos at $r > R_\nu$. The resulting net energy gain causes \dot{q} to increase sharply in the immediate neighborhood of $r = R_\nu$. However, the decrease of the neutrino heating rate due to the diminishing neutrino fluxes and any ν_e - ν_s and $\bar{\nu}_e$ - $\bar{\nu}_s$ oscillations takes effect at larger r . The above two competing factors cause \dot{q} to peak near the neutrinosphere. At even larger r corresponding to $T < 1$ MeV, formation of α -particles becomes important and the associated energy release results in the other peak of \dot{q} . At $T \gtrsim 1$ MeV, neutrino heating by the reactions in Eqs. (1a) and (1b) makes the dominant contribution to \dot{q} . As the rate of heating by these reactions is substantially reduced by ν_e - ν_s and $\bar{\nu}_e$ - $\bar{\nu}_s$ oscillations in case A, the \dot{q} in this case is significantly less than that in case D without oscillations. In order to drive the wind, the net energy gain must overcome the gravitational potential of the PNS (Qian & Woosley 1996). So the mass loss rate of the wind can be estimated as

$$\dot{M} \sim \frac{R_\nu}{GM_{\text{PNS}}} \int_{R_\nu}^{R_b} 4\pi r^2 \rho \dot{q} dr. \quad (25)$$

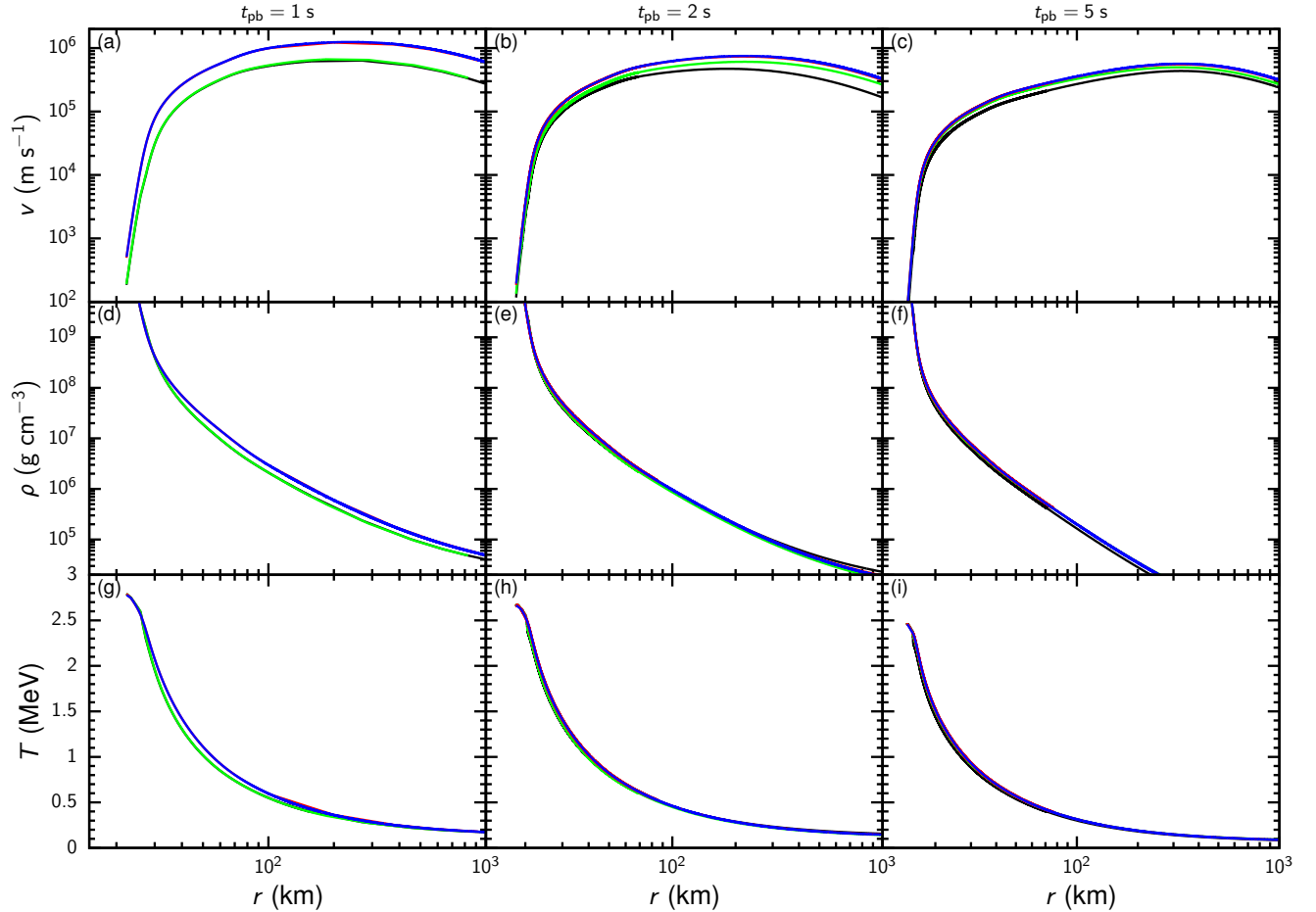


Figure 1. Wind profiles of v (upper row), ρ (central row), and T (bottom row) as functions of radius r at $t_{pb} = 1$ s (left column), 2 s (central column), and 5 s (right column) for cases A (black), B (green), C (red), and D (blue). Note that red and blue curves are indistinguishable.

The reduction of \dot{q} by oscillations in case A leads to the reduction of \dot{M} by a factor of ≈ 2.7 , 1.6, and 1.6 for $t_{pb} = 1$, 2, and 5 s, respectively, relative to case D (see Table 3).

Using $4\pi r^2 \rho \dot{q} = \dot{M} \dot{q}/v$, we can rewrite Eq. (25) as

$$\int_{R_\nu}^{R_b} \frac{\dot{q}}{v} dr \sim \frac{GM_{\text{PNS}}}{R_\nu}. \quad (26)$$

Because the right-hand side of the above equation is fixed for both cases with and without oscillations, the reduction of \dot{q} by oscillations in case A is expected to be accompanied by the reduction of v relative to case D (see Figs. 1(a)-(c)). With the reduced neutrino heating rate, the wind material in case A must move more slowly so that there is more time for the material to gain the energy required to overcome the gravitational potential of the PNS. We show \dot{q}/v as a function of r in Figs. 2(g)-(i). It can be seen that except for the region near the neutrinosphere where oscillations give rise to complicated behaviors in case A, \dot{q}/v is very similar for cases A and D.

Compared to v , the differences in the profile of ρ or T between cases A and D are much smaller (see Fig. 1). This result is expected for T because $T(R_\nu)$ and $T(R_b)$ are fixed at the inner and outer boundaries for all cases. Indeed, Fig. 3 shows that relative to case D, the reduction in the neutrino heating rate by oscillations in case A causes a decrease in T by at most $\sim 6\%$, 3% , and 4% for $t_{pb} = 1$, 2, and 5 s, respectively. This initial decrease is compensated as the slower wind material in case A gains energy at the reduced neutrino heating rate over a longer time than case D so that the same $T(R_b)$ is obtained. The similar profiles of T and \dot{q}/v for cases A and D result in similar profiles of

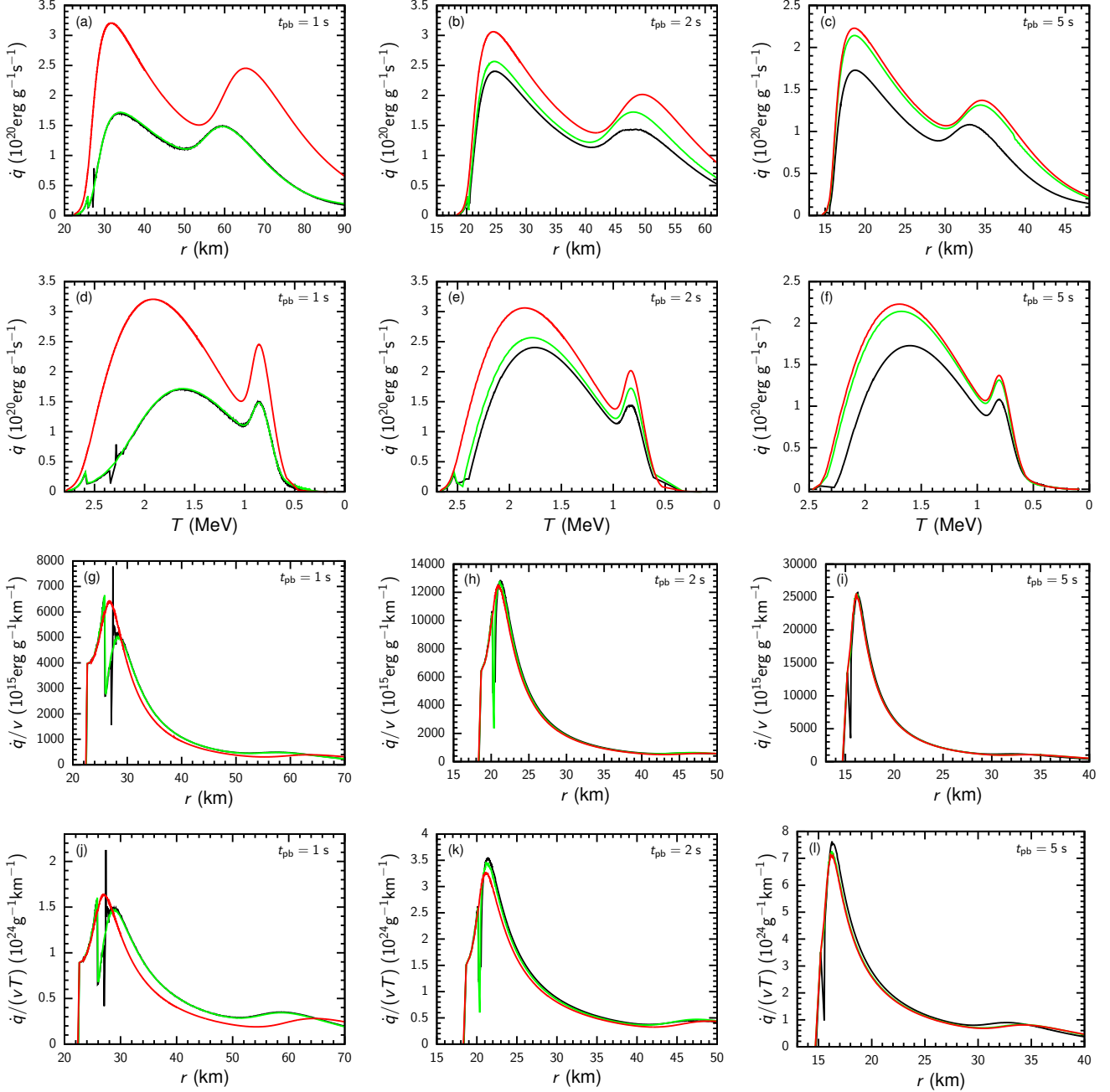


Figure 2. Net heating rates \dot{q} as functions of radius r (upper row) and temperature T (second row), as well as \dot{q}/v (third row) and $\dot{q}/(vT)$ (bottom row) as functions of r at $t_{pb} = 1$ s (left column), 2 s (central column), and 5 s (right column) for cases A (black), B (green), and C (red).

$\dot{q}/(vT)$ (see Figs. 2(j)-(l)). Because the total entropy per baryon S_{tot} as a function of r can be estimated as

$$S_{\text{tot}}(r) \sim S_{\text{tot}}(R_\nu) + \int_{R_\nu}^r \frac{m_u \dot{q}}{Tv} dr, \quad (27)$$

similar profiles of $\dot{q}/(vT)$ lead to similar profiles of S_{tot} for cases A and D. As shown in Fig. 4, relative to case D, the largest deviation of S_{tot} for case A is an increase by $\sim 16\%$, 5% , and 5% for $t_{pb} = 1, 2,$ and 5 s, respectively. Because $S_{\text{tot}}(r)$ mainly depends on T and ρ , being approximately $\propto T^3/\rho$ (Qian & Woosley 1996), similar profiles of S_{tot} and

T mean similar profiles of ρ as well. As $\dot{M} = 4\pi r^2 \rho v$, the reduction of \dot{M} by oscillations in case A mostly translates into the reduction of v relative to case D, which is in agreement with the discussion in the preceding two paragraphs.

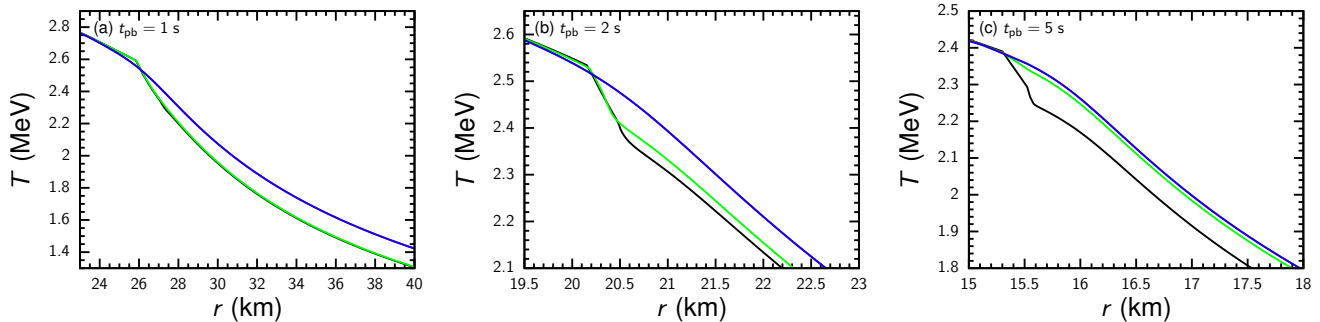


Figure 3. Wind temperature T near the onset of active-sterile neutrino oscillations as a function of radius r at $t_{\text{pb}} = 1$ s (a), 2 s (b), and 5 s (c) for cases A (black), B (green), C (red), and D (blue). Note that red and blue curves are indistinguishable.

3.2. Active-sterile neutrino oscillations and effects on the Y_e profile

In addition to the effects on the mass loss rates and profiles of v , ρ , and T discussed above, active-sterile neutrino oscillations can change the evolution of Y_e , which is critical to nucleosynthesis. Further, the intricate feedback between the evolution of Y_e and survival probabilities of ν_e and $\bar{\nu}_e$ leads to a range of interesting behaviors of active-sterile neutrino oscillations, which are presented below. For convenience, we denote the cases under discussion by the letter for the vacuum mixing parameters (see Table 1) followed by the numerical value of the t_{pb} for the snapshot (see Table 2). For example, case A1 refers to $\delta m^2 = 1.75$ eV², $\sin^2 2\theta_V = 0.10$, and $t_{\text{pb}} = 1$ s.

In Figs. 5(a)-(c) we show the Y_e profiles for all the cases. Because ν_e absorption on neutrons increases whereas $\bar{\nu}_e$ absorption on protons decreases Y_e , the change of Y_e due to active-sterile neutrino oscillations approximately follows the corresponding change of the ratio $\lambda_{\nu_e n}/\lambda_{\bar{\nu}_e p}$ for the rates of these reactions. This ratio is shown as a function of r in Figs. 5(d)-(f) for all the cases. Compared with the corresponding cases of no oscillations, cases C1, C2, and C5 show essentially no change of $\lambda_{\nu_e n}/\lambda_{\bar{\nu}_e p}$, and hence Y_e , up to $r \sim 90$, 60, and 40 km, respectively. Although $\lambda_{\nu_e n}/\lambda_{\bar{\nu}_e p}$ changes greatly at larger radii for these three cases, there are no corresponding changes of Y_e because Y_e has essentially frozen out at such large radii due to the small rates of the pertinent reactions. Therefore, active-sterile neutrino oscillations have negligible effects on the Y_e profiles in cases C1, C2, and C5. In contrast, there are significant changes of the Y_e profiles due to oscillations in all the other cases. With the exception of case A5, active-sterile neutrino oscillations in these cases reduce $\lambda_{\nu_e n}/\lambda_{\bar{\nu}_e p}$, and hence Y_e , relative to the corresponding cases of no oscillations. Case A5 is unique in that oscillations increase $\lambda_{\nu_e n}/\lambda_{\bar{\nu}_e p}$, and hence Y_e . Note again that Y_e eventually freezes out and do not track the effects of oscillations on $\lambda_{\nu_e n}/\lambda_{\bar{\nu}_e p}$ at large radii.

To understand the effects of active-sterile neutrino oscillations on $\lambda_{\nu_e n}$ and $\lambda_{\bar{\nu}_e p}$, we show in Figure 6 the average survival probabilities $\langle P_{\nu_e}(r) \rangle$ and $\langle P_{\bar{\nu}_e}(r) \rangle$ of ν_e and $\bar{\nu}_e$, respectively, as functions of r for all the relevant cases. Here for example,

$$\langle P_{\nu_e}(r) \rangle = \int P_{\nu_e}(E, r) f_{\nu_e}(E) dE, \quad (28)$$

where $f_{\nu_e}(E)$ is the normalized ν_e spectrum at emission [see Eq. (6)]. The flavor evolution of ν_e and $\bar{\nu}_e$ is sensitive to the Mikheyev-Smirnov-Wolfenstein-like (MSW-like) resonances (Wolfenstein 1978; Mikheev & Smirnov 1985) corresponding to

$$V_{\text{tot}}(r) = V_{\text{mat}}(r) + V_{\nu}(r) = \pm \frac{\delta m^2}{2E} \cos 2\theta_V, \quad (29)$$

where the plus and minus signs are for ν_e - ν_s and $\bar{\nu}_e$ - $\bar{\nu}_s$ oscillations, respectively. In the above equation, V_{tot} is the total effective potential for flavor evolution with contributions V_{mat} [Eq. (22)] and V_{ν} [Eq. (24)] from neutrino forward scattering on matter particles and other neutrinos, respectively. As a first approximation, the radii for the resonances can be estimated from

$$V_{\text{mat}}(r) = \frac{\sqrt{2}G_F}{2m_u} \rho(r) [3Y_e(r) - 1] \sim \pm \frac{\delta m^2}{2E} \cos 2\theta_V. \quad (30)$$

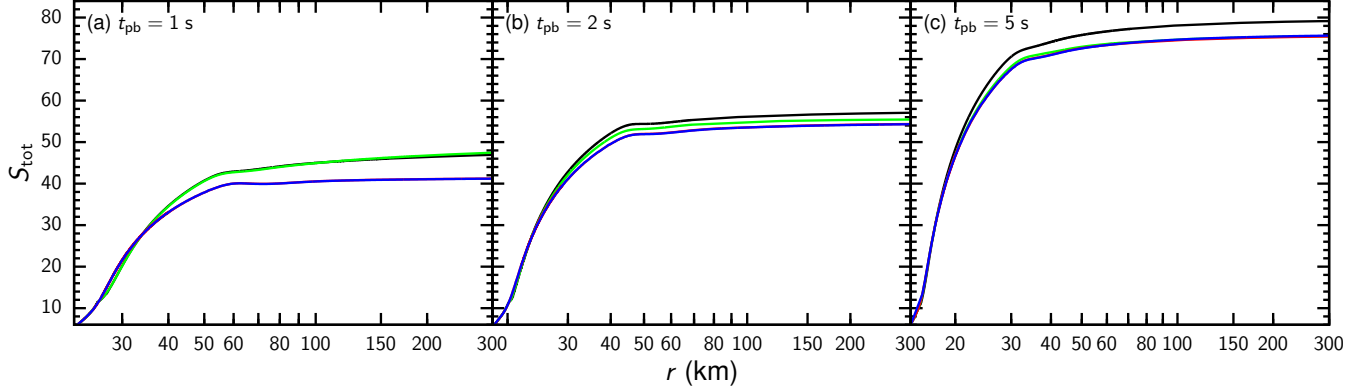


Figure 4. Total entropy S_{tot} as a function of radius r at $t_{\text{pb}} = 1$ s (a), 2 s (b), and 5 s (c) for cases A (black), B (green), C (red), and D (blue). Note that red and blue curves are indistinguishable.

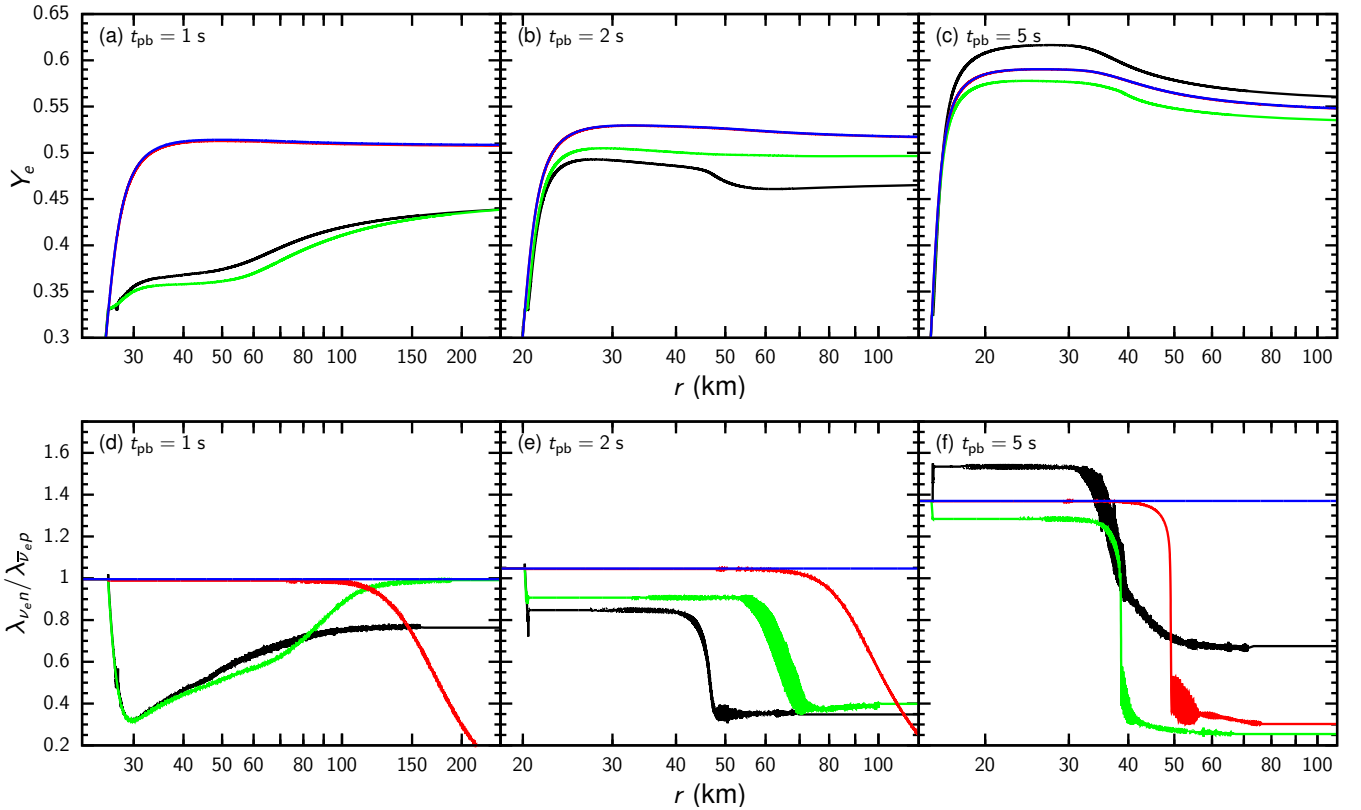


Figure 5. Electron fraction Y_e (upper row) and ratio of the rates $\lambda_{\nu_e n} / \lambda_{\nu_e p}$ (bottom row) as functions of radius r at $t_{\text{pb}} = 1$ s (left column), 2 s (central column), and 5 s (right column) for cases A (black), B (green), C (red), and D (blue). Note that the red and blue curves for Y_e are indistinguishable.

The term $\rho(3Y_e - 1)$ in V_{mat} gives rise to two types of resonances. The inner resonances occur for both $\nu_e - \nu_s$ and $\bar{\nu}_e - \bar{\nu}_s$ oscillations close to the neutrinosphere as Y_e increases from below to slightly above $1/3$. Here $G_F \rho / m_u$ far exceeds $\delta m^2 / E$ and the resonance conditions are met in the region with $Y_e \sim 1/3$. In contrast, the outer resonances occur only for $\nu_e - \nu_s$ oscillations at much larger radii. Here Y_e is significantly above $1/3$ and the resonance condition is met only for the upper sign in Eq. (30) due to the much smaller ρ .

The main features of oscillations in cases C1, C2, and C5 are the two types of resonances outlined above. Using V_{tot} instead of V_{mat} in the resonance conditions does not change the discussion qualitatively except for the outer resonance in case C5. As shown in Fig. 7, for a fixed ν_e or $\bar{\nu}_e$ energy, the inner resonance condition is met at a slightly

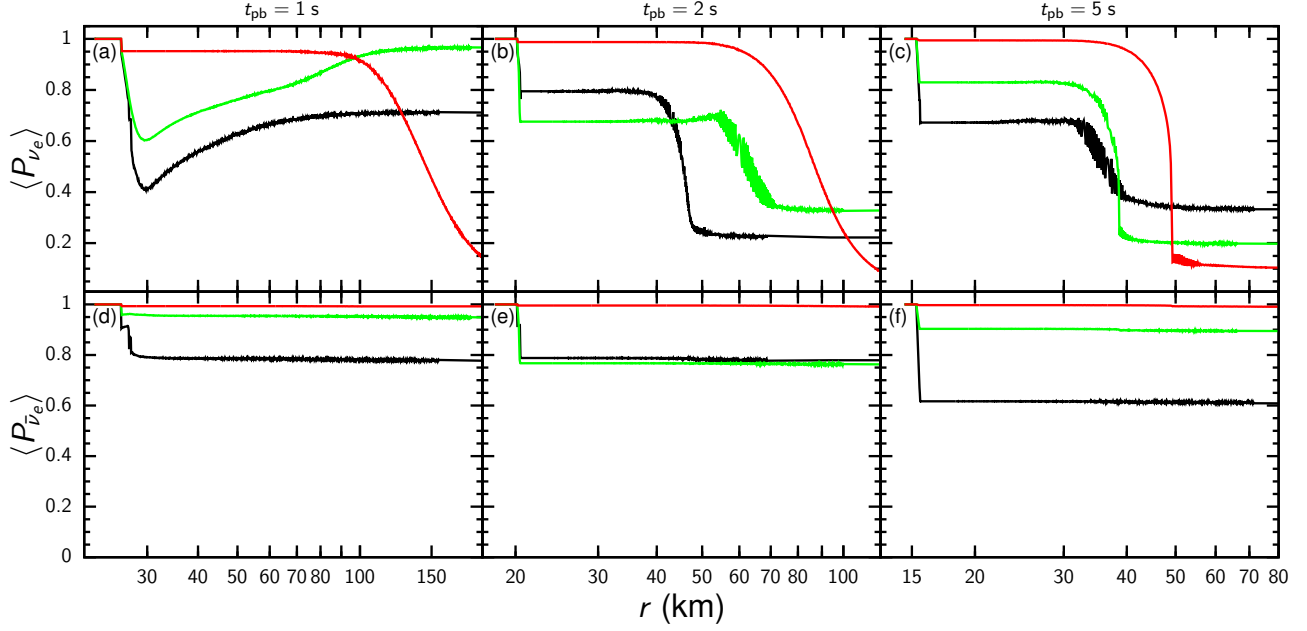


Figure 6. Average survival probabilities for ν_e and $\bar{\nu}_e$ as functions of radius at $t_{pb} = 1$ s (left column), 2 s (central column), and 5 s (right column) for cases A (black), B (green), and C (red).

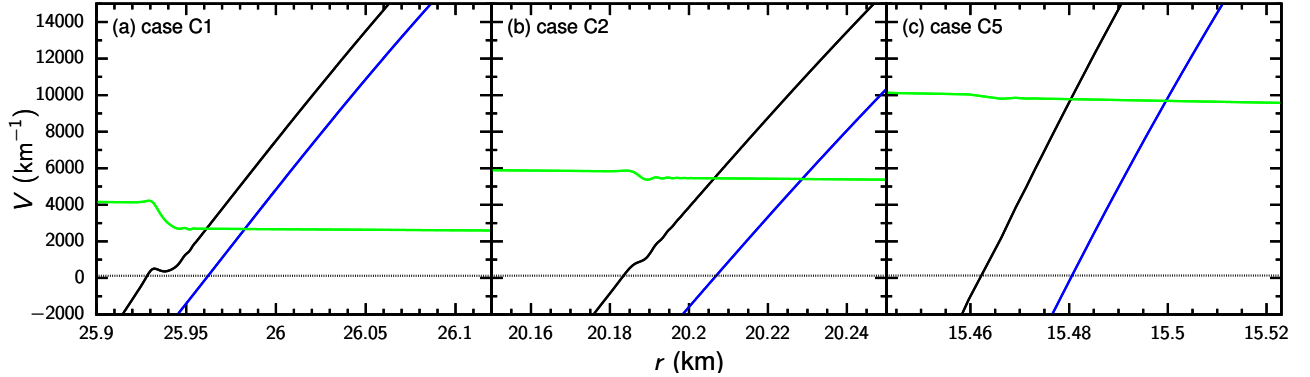


Figure 7. Effective potentials V_{tot} (solid black), V_{mat} (solid blue), and V_ν (solid green) as functions of radius r near the inner resonances at $t_{pb} = 1$ s (a), 2 s (b), and 5 s (c) for case C. For comparison, dotted black lines correspond to $\delta m^2 / (2 \langle E_{\nu_e} \rangle)$.

smaller r when V_{tot} is used. With the small values of the corresponding δm^2 and $\sin^2 2\theta_V$, flavor evolution through the inner resonances is rather non-adiabatic for ν_e and $\bar{\nu}_e$ of typical energies, which leads to large $\langle P_{\nu_e}(r) \rangle$ and $\langle P_{\bar{\nu}_e}(r) \rangle$ immediately following the inner resonances in cases C1, C2, and C5 (see Fig. 6). Using V_{tot} again changes only slightly the radius of the outer resonance for a specific ν_e energy in cases C1 and C2 (see Figs. 8(a)-(b)). Because V_{tot} changes much more slowly at large radii, ν_e flavor evolution through the outer resonances is rather adiabatic, which results in large decrease of $\langle P_{\nu_e}(r) \rangle$ following the outer resonances in cases C1 and C2 (see Figs. 6(a)-(b)). The outer resonance in case C5 becomes qualitatively different when V_{tot} is used. Here the magnitude of V_ν becomes comparable to that of V_{mat} and V_{tot} essentially becomes flat (see Fig. 8(c)). This behavior resembles that of the matter-neutrino resonances for active-active neutrino oscillations (e.g., Malkus et al. 2016; Wu et al. 2016a), and results in efficient conversion of ν_e with typical energies in case C5 (see Fig. 6(c)). However, because the outer resonances occur after the freeze-out of Y_e , they have little impact on the Y_e profiles. Therefore, active-sterile neutrino oscillations in cases C1, C2, and C5 only have small effects on all the wind properties, and will not be discussed any further.

As can be seen clearly in Fig. 6(b)-(c), the outer resonances also occur to further decrease $\langle P_{\nu_e}(r) \rangle$ in cases A2, B2, A5, and B5. For case B2, the outer resonances are similar to those in case C2. For cases A2, A5, and B5, V_ν becomes

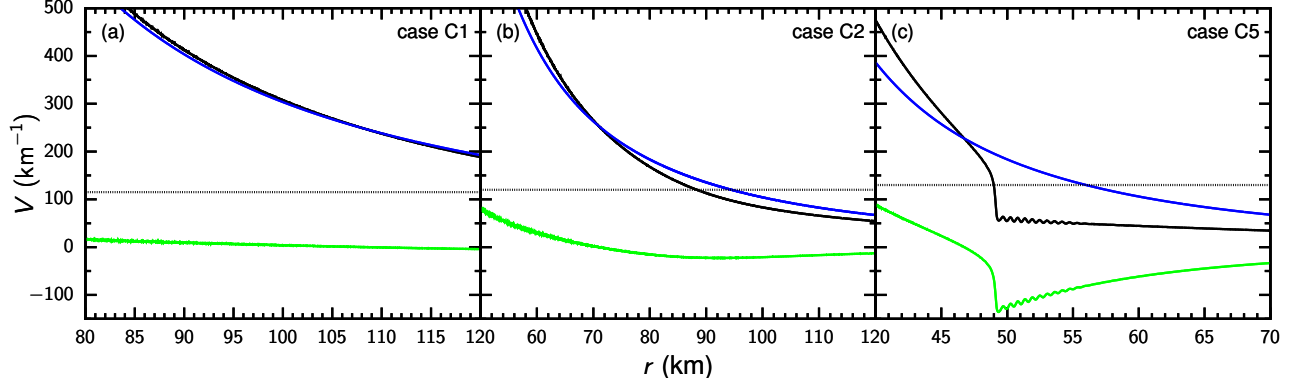


Figure 8. Effective potentials V_{tot} (solid black), V_{mat} (solid blue), and V_{ν} (solid green) as functions of radius r near the outer resonances at $t_{\text{pb}} = 1$ s (a), 2 s (b), and 5 s (c) for case C. For comparison, dotted black lines correspond to $\delta m^2 / (2 \langle E_{\nu_e} \rangle)$.

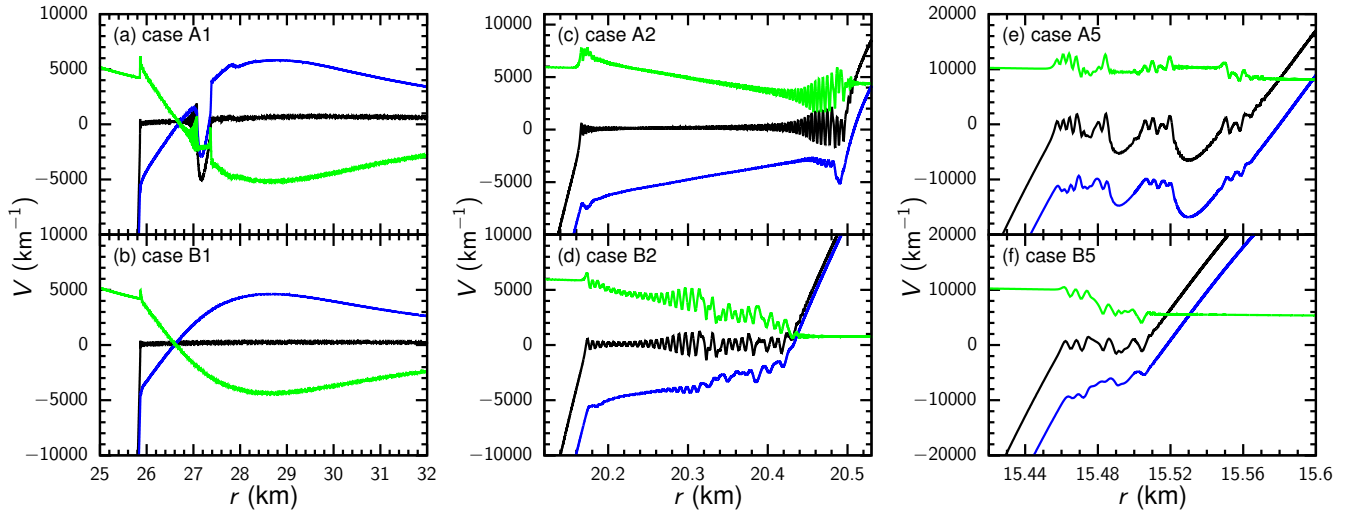


Figure 9. Effective potentials V_{tot} (black), V_{mat} (blue), and V_{ν} (green) as functions of radius r near the inner resonances at $t_{\text{pb}} = 1$ s (left column), 2 s (central column), and 5 s (right column) for cases A (top row) and B (bottom row).

significant and the behavior of the outer resonances starts to approach that in case C5. However, all outer resonances occur at large radii corresponding to small rates of the pertinent neutrino reactions. Consequently, their effects on the Y_e profiles and other wind properties are very limited. Below we focus on the inner resonances, which dominate the overall flavor evolution in cases A1 and B1 as well as produce in general the predominant effects of active-sterile neutrino oscillations on all the wind properties including the Y_e profiles.

A full understanding of the inner resonances for ν_e - ν_s and $\bar{\nu}_e$ - $\bar{\nu}_s$ oscillations requires a careful examination of how the conditions in Eq. (29) are fulfilled by the contributions V_{mat} and V_{ν} to V_{tot} . These quantities are shown as functions of r for cases A1, B1, A2, B2, A5, and B5 in Fig. 9. All these cases have significant plateaus of $V_{\text{tot}} \sim \pm \delta m^2 \cos 2\theta_V / (2E)$ corresponding to inner resonances for ν_e and $\bar{\nu}_e$ of typical energies. These plateaus can be divided into three categories: (1) a stable plateau spanning > 1 km as in case B1, (2) an unstable one spanning ~ 0.1 – 0.3 km as in cases A2, B2, A5, and B5, and (3) a wide one interrupted by an instability as in case A1. For all three categories, the plateau results from the near cancellation of V_{mat} and V_{ν} , each of which has a magnitude far exceeding that of V_{tot} for the most part of the corresponding region. The Y_e in this region is nearly constant and stays close to $1/3$. This dramatic flattening of the Y_e profile corresponding to the inner resonances is shown for case A2 as an example in Fig. 10.

Formation of the plateau of V_{tot} merits a detailed followup study. Here we only offer a qualitative sketch of the possible underlying mechanism as illustrated in Fig. 11. The total potential V_{tot} and the vacuum mixing parameters δm^2 and $\sin^2 2\theta_V$ control the flavor evolution of ν_e and $\bar{\nu}_e$, mostly through the occurrence of resonances. This evolution determines the survival probabilities P_{ν_e} and $P_{\bar{\nu}_e}$, which immediately modify the contribution V_{ν} from neutrino forward

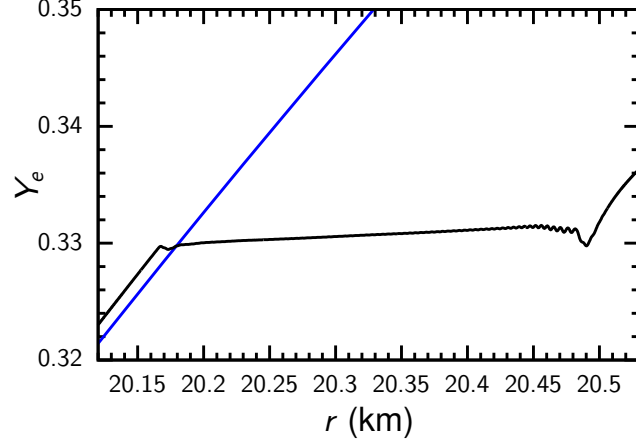


Figure 10. Profiles of electron fraction Y_e as functions of radius r near the inner resonances at $t_{pb} = 2$ s for cases A (black) and D (blue).

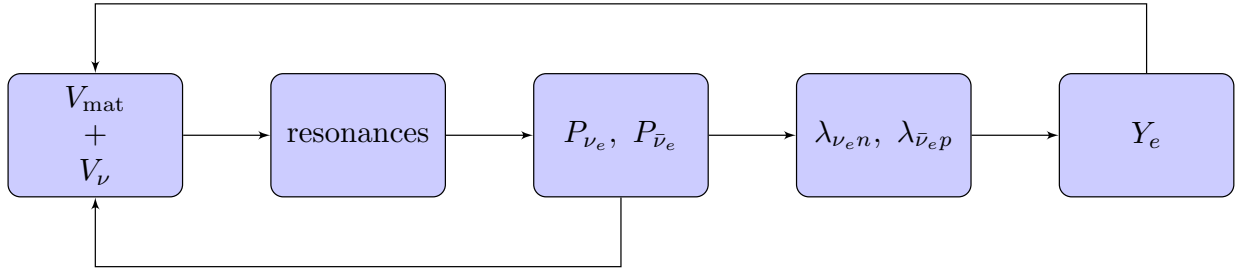


Figure 11. Sketch of the feedback loops for active-sterile neutrino oscillations in the wind. See text for detail.

scattering on other neutrinos to V_{tot} . The above factors form the first feedback loop of flavor evolution. In addition, P_{ν_e} and $P_{\bar{\nu}_e}$ directly modify the rates $\lambda_{\nu_e n}$ and $\lambda_{\bar{\nu}_e p}$, which control the evolution of Y_e . In turn, Y_e determines the contribution V_{mat} from neutrino forward scattering on matter particles to V_{tot} . These factors form the second feedback loop of flavor evolution. Clearly, the first loop would not operate were V_ν far smaller than V_{mat} in magnitude, and the second loop would not operate if $\lambda_{\nu_e n}$ and $\lambda_{\bar{\nu}_e p}$ were too small to change Y_e significantly. Consequently, both loops become ineffective at sufficiently large radii, where V_ν , $\lambda_{\nu_e n}$, and $\lambda_{\bar{\nu}_e p}$ are too small due to the geometric dilution of neutrino fluxes. In contrast, both loops are expected to be efficient close to the neutrinosphere, thereby forming the plateau of V_{tot} for the inner resonances. However, instabilities appear to develop in the feedback loops under some conditions. Whether and how these instabilities can develop under different conditions might explain the three categories of plateaus presented above. We plan to investigate the feedback loops and associated instabilities in the followup study. We also note that those outer resonances similar to the matter-neutrino resonances (e.g., as shown in Fig. 8(c) for case C5) are governed by only the first feedback loop described above.

4. RESULTS ON NUCLEOSYNTHESIS

In this section, we discuss the impact of active-sterile neutrino oscillations on the production of heavy elements in neutrino-driven winds. From our wind models, we take a specific set of v , ρ , and T profiles and use $dt = dr/v$ to define the evolution of $\rho(t)$ and $T(t)$ for a mass element as it moves through the wind. We use the same established nuclear reaction network as in Wu et al. (2016b) to calculate the evolution of the number fraction, or abundance, of each nucleus. We start the network calculation at an initial temperature of $T = 20$ GK, for which the nuclear composition is dominated by free nucleons. We take the detailed nuclear abundances from the NSE involving all the nuclei in the network for $20 \geq T \geq 10$ GK when NSE holds very well, and evolve the nuclear abundances with the full reaction network for $T < 10$ GK. Throughout the nucleosynthesis calculations, we follow the evolution of Y_e using the rates of ν_e and $\bar{\nu}_e$ absorption and e^\pm capture on free nucleons as calculated by the wind models. The resulting evolution of $Y_e(t)$ is in excellent agreement with that calculated directly from the wind models, which always assume a simple NSE

composition with free nucleons and α -particles only. We have also checked that \dot{q}_α , the rate of energy gain per unit mass from α -particle formation used in the wind models, is a good approximation based on the evolution of nuclear abundances in the network calculations. Therefore, the simple nuclear composition assumed in the wind models is sufficiently accurate for modeling the wind dynamics and the evolution of Y_e .

For the evolution of $\rho(t)$ and $T(t)$ covered by all our wind models, the Y_e values at $T \lesssim 5$ GK are critical to the nucleosynthesis. A more convenient parameter is the corresponding neutron excess $\delta = 1 - 2Y_e$. For $Y_e \sim 0.5$ with $|\delta| \lesssim 0.02$, mainly the Fe group nuclei (mass numbers of $A \sim 56$ and atomic numbers of $Z \sim 28$) are produced. For $Y_e > 0.5$ with $\delta < -0.02$, the wind is sufficiently proton-rich and the nuclear flow proceeds beyond the Fe group nuclei through the νp -process (Frohlich et al. 2006). During this process, $\bar{\nu}_e$ absorption on protons can maintain a significant neutron abundance to facilitate (n, p) reactions after reactions between charged particles freeze out. In contrast, for $Y_e < 0.5$ with $\delta > 0.02$, the wind is sufficiently neutron-rich and the nuclear flow proceeds beyond the Fe group nuclei much more efficiently through the α -process (Woosley & Hoffman 1992).

Figure 12 shows the final abundances produced in all our wind models as functions of mass number A (left panels) and atomic number Z (middle panels), respectively. In the absence of neutrino oscillations, the wind is generally proton-rich and becomes more so for the later epochs of the CCSN evolution, with typical values of $Y_e \sim 0.51, 0.52$, and 0.55 for cases D1, D2, and D5, respectively (see Fig. 5). Consequently, nucleosynthesis shifts from dominant production of Fe group nuclei for case D1 to increasing production of heavier nuclei through the νp -process for cases D2 and D5. This trend is more clearly shown in the right panels of Fig. 12 in terms of the logarithmic production factor $[X] = \log(X/X_\odot)$, where X is the mass fraction of a nucleus produced in the wind and X_\odot is the corresponding value in the solar system. For understanding how the solar composition is obtained by mixing the nucleosynthesis contributions from various astrophysical sources, values of $[X]$ are more important than the abundances produced by a source. For example, ^{45}Sc has the highest value of $[X] \approx 2.3$ among all the nuclei produced by the wind in case D1, while ^{56}Fe has the highest abundance but a much smaller value of $[X] \approx 0.9$. This result means that even if all the ^{45}Sc in the solar system came from sources like this wind, these sources could have contributed only $\approx 4\%$ of the solar ^{56}Fe . The horizontal bands in Figs. 12-13 indicate $[X]$ within 1 dex of the highest value. Nuclei within these bands would be the most relevant for contributions to the solar composition.

Because active-sterile neutrino oscillations have little impact on the Y_e profiles in cases C1, C2, and C5, nucleosynthesis in these cases is essentially identical to that in the corresponding cases of no oscillations. In addition, all cases have similar nucleosynthesis for $t_{\text{pb}} = 5$ s because the corresponding winds are similarly proton-rich (see Fig. 12). In contrast, oscillations greatly reduce the Y_e values in cases A1, B1, and A2 (see Fig. 5), and dramatically alter the nucleosynthesis to produce nuclei far beyond the Fe group (see Fig. 12). The largest $[X]$ is ≈ 5.5 and 5.4 for ^{86}Kr in cases A1 and B1, respectively, and is ≈ 5.1 for ^{90}Zr in case A2 (see Fig. 13). Both nuclei have a magic number (50) of neutrons and are produced by the α -process. Finally, oscillations also reduce Y_e significantly in case B2, but the resulting values of $Y_e \sim 0.5$ correspond to a very small $|\delta|$. Consequently, case B2 has the least extensive production of nuclei beyond the Fe group among all the cases for $t_{\text{pb}} = 2$ s. Specifically, ^{62}Ni and ^{58}Ni have the largest two $[X]$ values of ≈ 2.2 and 1.9 , respectively, in this case, while ^{45}Sc and ^{72}Ge have the largest two $[X]$ values of ≈ 2.4 and 2.1 , respectively, in case D2.

5. CONCLUSIONS

We have included active-sterile neutrino oscillations in a steady-state model of the neutrino-driven wind and self-consistently treated the effects of oscillations on the v , ρ , T , and Y_e profiles of the wind. Compared to previous studies (e.g., Nunokawa et al. 1997; McLaughlin et al. 1999; Tamborra et al. 2012; Wu et al. 2014; Pllumbi et al. 2015) that addressed only the effects on the Y_e profile, our study represents a significant step forward. Among the three sets of vacuum mixing parameters adopted here (see Table 1), we find that only those of case C with $\delta m^2 = 0.4$ eV² produce negligible effects on the wind. In contrast, those of cases A and B with $\delta m^2 = 1.75$ and 1.0 eV², respectively, significantly change the wind dynamics in addition to the Y_e profile. Specifically, the mass loss rate is reduced by a factor of $\approx 2.7, 1.6$, and 1.6 for $t_{\text{pb}} = 1, 2$, and 5 s in cases A1, A2, and A5, respectively (see Table 3). This reduction translates into a similar reduction of the wind velocity and is caused by the reduced heating as ν_e and $\bar{\nu}_e$ are converted into their sterile counterparts. While the effects of oscillations on the ρ and T profiles are much smaller, the resulting increases in S_{tot} by $\sim 15\%, 5\%$, and 5% in cases A1, A2, and A5, respectively (see Fig. 4), are still noticeable.

With respect to nucleosynthesis, the most important effects of active-sterile neutrino oscillations are the resulting changes of Y_e , which range from significant in cases B2, A5, and B5 to large in cases A1, B1, and A2 (see Fig. 5). With

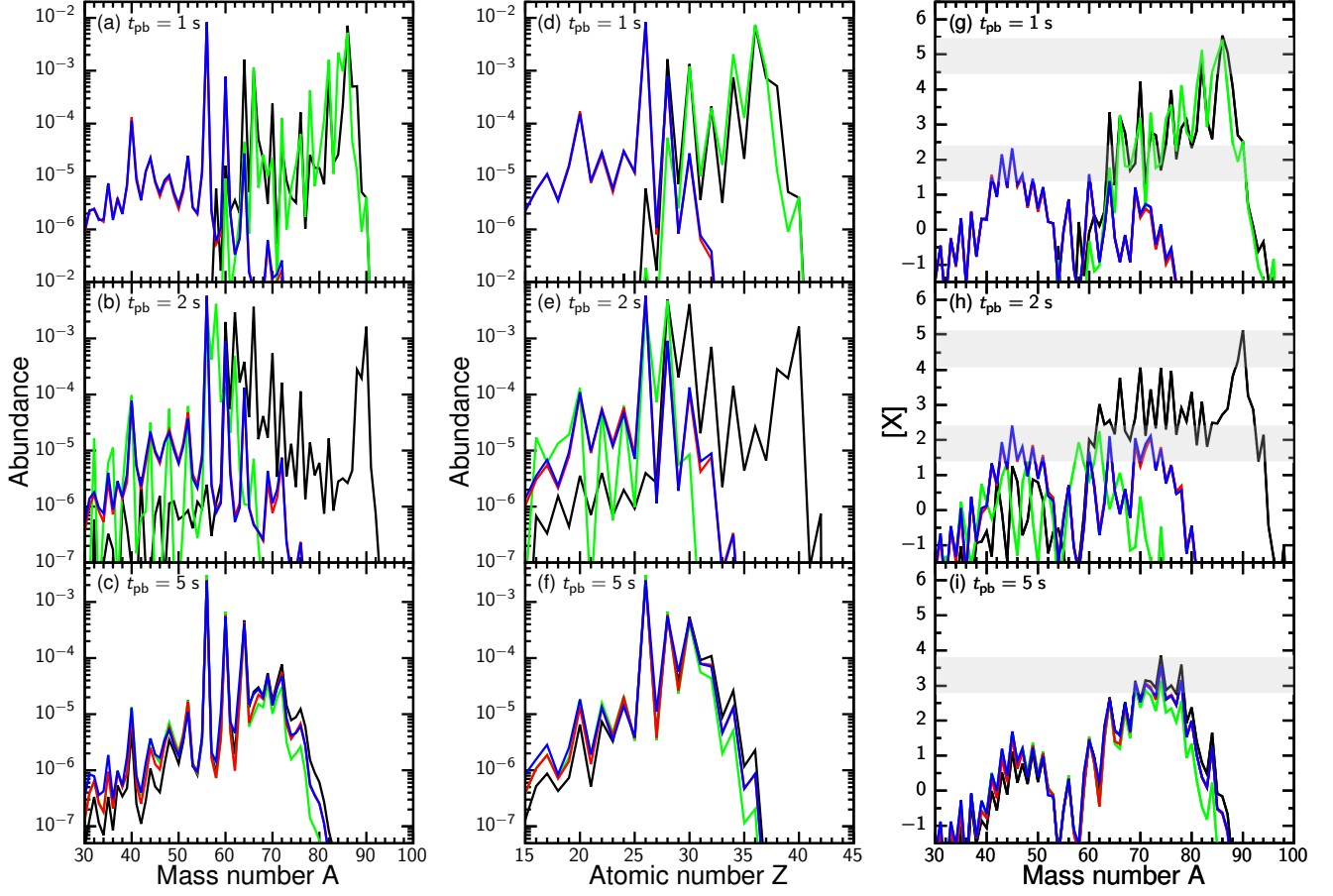


Figure 12. Abundances as functions of mass number (left column) and atomic number (central column), as well as logarithmic production factors as functions of mass number (right column) at $t_{pb} = 1$ s (upper row), 2 s (central row), and 5 s (bottom row) for cases A (black), B (green), C (red), and D (blue). The effective production band is indicated by the grey region in the right column. Note that red and blue curves are almost indistinguishable.

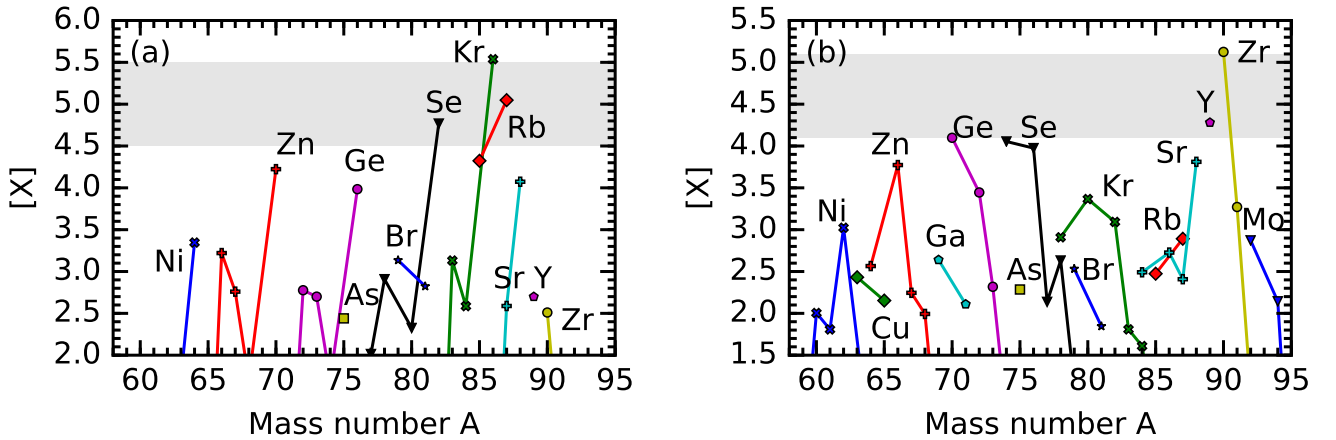


Figure 13. Production factors as functions of mass number for case A at $t_{pb} = 1$ s (a) and 2 s (b). Isotopes of the same element are connected by line segments. The effective production band is indicated by the grey region.

the large reduction of Y_e in the latter three cases, nucleosynthesis is dramatically altered (see Figs. 12-13). For cases D1

and D2 with no oscillations, the final abundance pattern is characterized by the largest $[X] \approx 2.3$ and 2.4, respectively, for ^{45}Sc . In contrast, ^{86}Kr is produced with the largest $[X] \approx 5.5$ and 5.4 in cases A1 and B1, respectively, and ^{90}Zr is produced with the largest $[X] \approx 5.1$ in case A2. Not only do oscillations change the dominant nuclei produced in these cases, but they also greatly amplify the potential contributions from the corresponding winds to the solar composition. The effects of oscillations are also large but less dramatic in case B2, where ^{62}Ni is produced with the largest $[X] \approx 2.2$ (see Fig. 12). On the other hand, oscillations do not change the nucleosynthesis very much in cases A5 and B5 despite the significant changes of Y_e (see Fig. 12). This result comes about because the Y_e in these cases corresponds to a proton-rich wind that undergoes the νp -process similar to the case of no oscillations. We conclude that active-sterile neutrino oscillations with vacuum mixing parameters similar to those in cases A and B can greatly affect nucleosynthesis in the winds at the early epochs of $t_{\text{pb}} \sim 1\text{--}2$ s during the CCSN evolution.

In agreement with previous studies (e.g., Wu et al. 2014), we find that active-sterile neutrino oscillations near the PNS exhibit features beyond the usual MSW effect that is dominated by the potential V_{mat} from neutrino forward scattering on matter particles. These interesting features are caused by the potential V_ν from neutrino forward scattering on other neutrinos, and more importantly, by the feedback of oscillations on both V_{mat} and V_ν (see Fig. 11). In particular, we have observed plateau-like behaviors of $V_{\text{tot}} = V_{\text{mat}} + V_\nu$ for the outer MSW-like resonances in case C5 (see Fig. 8(c)) and for the inner resonances in all the wind models with vacuum mixing parameters of cases A and B (see Fig. 9). We have given only a qualitative explanation of such behaviors here, and plan to investigate them in detail in a followup study. In addition, we have made some simplifying approximations in our present study. For example, we have assumed that all active neutrinos are emitted from the same sharp neutrinosphere. In reality, where neutrinos decouple from matter depends on the neutrino species and energy. Although using slightly different neutrinospheres for ν_e , $\bar{\nu}_e$, and ν_x ($\bar{\nu}_x$) is more realistic, we do not expect that this modification would affect our results qualitatively. Nevertheless, we also plan to check the effects of this and other possible improvements of our model in the followup study.

We thank Gabriel Martínez-Pinedo for discussion during the initial phase of our study. We also acknowledge the Minnesota Supercomputing Institute at the University of Minnesota for providing resources that contributed to the research results reported here. This work was supported in part by the US Department of Energy [DE-FG02-87ER40328 (UM)], the Ministry of Science and Technology of Taiwan [107-2119-M-001-038 (IOP)], the National Natural Science Foundation of China [11533006, 11655002 (TDLI)], and the Science and Technology Commission of Shanghai Municipality [16DZ2260200 (TDLI)].

APPENDIX

A. RATES OF NEUTRON-PROTON INTERCONVERSION AND OF ENERGY GAINS AND LOSSES

The rate $\lambda_{\nu_e n}$ is given by Eq. (13b). Using the same notation, we can write $\lambda_{\bar{\nu}_e p}$ as

$$\lambda_{\bar{\nu}_e p} = \frac{G_F^2 |V_{ud}|^2 (1 + 3g_A^2)}{2\pi^2} \frac{L_{\bar{\nu}_e} D(r)}{R_\nu^2 \langle E_{\bar{\nu}_e} \rangle} \int_{E_{\text{th}}}^\infty (E - \Delta)^2 \left(1 - \frac{W_{\bar{\nu}_e} E}{m_N}\right) f_{\bar{\nu}_e}(E) P_{\bar{\nu}_e}(E, r) dE, \quad (\text{A1})$$

where $E_{\text{th}} = \Delta + m_e$ is the threshold $\bar{\nu}_e$ energy for absorption on protons, m_e is the electron rest mass, and

$$W_{\bar{\nu}_e} = \frac{2[1 + 5g_A^2 + 2g_A(1 + f_2)]}{1 + 3g_A^2}. \quad (\text{A2})$$

In the above equations, $V_{ud} = 0.974$, $g_A = 1.27$, and $f_2 = 3.71$. The rates λ_{e+n} and λ_{e-p} are

$$\lambda_{e+n} = \frac{G_F^2 |V_{ud}|^2 (1 + 3g_A^2)}{2\pi^3} T^5 \left[g_{0,2,0} \left(\frac{m_e}{T}, \eta, \frac{\Delta}{T}, 0 \right) - \frac{W_{\bar{\nu}_e} T}{m_N} g_{1,2,0} \left(\frac{m_e}{T}, \eta, \frac{\Delta}{T}, 0 \right) \right], \quad (\text{A3})$$

$$\lambda_{e-p} = \frac{G_F^2 |V_{ud}|^2 (1 + 3g_A^2)}{2\pi^3} T^5 \left[g_{0,2,0} \left(\frac{\Delta}{T}, -\eta, -\frac{\Delta}{T}, 0 \right) - \frac{W_{\nu_e} T}{m_N} g_{1,2,0} \left(\frac{\Delta}{T}, -\eta, -\frac{\Delta}{T}, 0 \right) \right], \quad (\text{A4})$$

respectively, where $\eta = \mu/T$, μ is the electron chemical potential, and

$$g_{i,j,k}(x_{\text{th}}, y, z, w) = \int_{x_{\text{th}}}^\infty \frac{x^{i+1} (x+z)^j (x+w)^k \sqrt{x^2 - (m_e/T)^2}}{\exp(x+y) + 1} dx. \quad (\text{A5})$$

The rates $\dot{q}_{\nu_e n}$ and $\dot{q}_{\bar{\nu}_e p}$ are

$$\dot{q}_{\nu_e n} = \frac{Y_n G_F^2 |V_{ud}|^2 (1 + 3g_A^2)}{m_u} \frac{L_{\nu_e} D(r)}{R_\nu^2 \langle E_{\nu_e} \rangle} \int_0^\infty [E + (\Delta - m_e)] (E + \Delta)^2 \left(1 - \frac{W_\nu E}{m_N}\right) f_{\nu_e}(E) P_{\nu_e}(E, r) dE, \quad (\text{A6})$$

$$\dot{q}_{\bar{\nu}_e p} = \frac{Y_p G_F^2 |V_{ud}|^2 (1 + 3g_A^2)}{m_u} \frac{L_{\bar{\nu}_e} D(r)}{R_\nu^2 \langle E_{\bar{\nu}_e} \rangle} \int_{E_{\text{th}}}^\infty [E - (\Delta - m_e)] (E - \Delta)^2 \left(1 - \frac{W_{\bar{\nu}_e} E}{m_N}\right) f_{\bar{\nu}_e}(E) P_{\bar{\nu}_e}(E, r) dE, \quad (\text{A7})$$

respectively. The rates \dot{q}_{e+n} and \dot{q}_{e-p} are

$$\dot{q}_{e+n} = \frac{Y_n G_F^2 |V_{ud}|^2 (1 + 3g_A^2)}{m_u} T^6 \left[g_{0,2,1} \left(\frac{m_e}{T}, \eta, \frac{\Delta}{T}, \frac{m_e}{T} \right) - \frac{W_{\bar{\nu}_e} T}{m_N} g_{1,2,1} \left(\frac{m_e}{T}, \eta, \frac{\Delta}{T}, \frac{m_e}{T} \right) \right], \quad (\text{A8})$$

$$\dot{q}_{e-p} = \frac{Y_p G_F^2 |V_{ud}|^2 (1 + 3g_A^2)}{m_u} T^6 \left[g_{0,2,1} \left(\frac{\Delta}{T}, -\eta, -\frac{\Delta}{T}, -\frac{m_e}{T} \right) - \frac{W_{\nu_e} T}{m_N} g_{1,2,1} \left(\frac{\Delta}{T}, -\eta, -\frac{\Delta}{T}, -\frac{m_e}{T} \right) \right], \quad (\text{A9})$$

respectively.

The rates given above are the most important for modeling the neutrino-driven wind, and therefore, are calculated with a higher accuracy. The other rates for energy gains and losses are less important. We adopt similar estimates of these rates to those in [Thompson et al. \(2001\)](#) but ignore the effects of general relativity. These approximate rates are given below.

The rate $\dot{q}_{\nu_e N}$ is

$$\dot{q}_{\nu_e N} = \frac{\kappa_n Y_n + \kappa_p Y_p}{m_u} \frac{G_F^2 L_{\nu_e} D(r)}{2\pi^2 R_\nu^2 \langle E_{\nu_e} \rangle} \int_0^\infty E^3 (E - 6T) f_{\nu_e}(E) P_{\nu_e}(E, r) dE, \quad (\text{A10})$$

where $\kappa_n = \frac{1}{4}(1 + 3g_A^2)$, $\kappa_p = (\frac{1}{2} - 2\sin^2\theta_W)^2 + \frac{3}{4}g_A^2$, and $\sin^2\theta_W = 0.231$. The above rate can be adapted in a straightforward manner to give $\dot{q}_{\bar{\nu}_e N}$, $\dot{q}_{\nu_x N}$, and $\dot{q}_{\bar{\nu}_x N}$. Note that all active neutrinos and antineutrinos of the same energy have the same cross sections for neutral-current scattering on nucleons.

The rate $\dot{q}_{\nu_e e^\pm}$ is

$$\dot{q}_{\nu_e e^\pm} = [\Lambda_{\nu_e e^-} n_{e^-} + \Lambda_{\nu_e e^+} n_{e^+}] \frac{G_F^2 T L_{\nu_e} D(r)}{2\pi^2 \rho R_\nu^2 \langle E_{\nu_e} \rangle} \int_0^\infty E(E - 4T) f_{\nu_e}(E) P_{\nu_e}(E, r) dE, \quad (\text{A11})$$

where $n_{e^\pm} = (T^3/\pi^2)g_{0,0,0}(m_e/T, \pm\eta, 0, 0)$ are the number densities of positrons and electrons, respectively, $\Lambda_{\nu_e e^-} = (C_V + C_A)^2 + \frac{1}{3}(C_V - C_A)^2$, $\Lambda_{\nu_e e^+} = (C_V - C_A)^2 + \frac{1}{3}(C_V + C_A)^2$, $C_V = \frac{1}{2} + 2\sin^2\theta_W$, and $C_A = \frac{1}{2}$. In adapting the above rate to give $\dot{q}_{\bar{\nu}_e e^\pm}$, $\dot{q}_{\nu_x e^\pm}$, and $\dot{q}_{\bar{\nu}_x e^\pm}$, note that $\Lambda_{\bar{\nu}_e e^-} = \Lambda_{\nu_e e^+}$, $\Lambda_{\bar{\nu}_e e^+} = \Lambda_{\nu_e e^-}$, $\Lambda_{\nu_x e^-} = (C_V + C_A - 2)^2 + \frac{1}{3}(C_V - C_A)^2$, $\Lambda_{\nu_x e^+} = (C_V - C_A)^2 + \frac{1}{3}(C_V + C_A - 2)^2$, $\Lambda_{\bar{\nu}_x e^-} = \Lambda_{\nu_x e^+}$, and $\Lambda_{\bar{\nu}_x e^+} = \Lambda_{\nu_x e^-}$.

The rate $\dot{q}_{\nu_e \bar{\nu}_e}$ is

$$\dot{q}_{\nu_e \bar{\nu}_e} = \frac{\Lambda_{\nu_e \bar{\nu}_e}}{\rho} \frac{G_F^2 L_{\nu_e} L_{\bar{\nu}_e} \Psi(r)}{36\pi^3 R_\nu^4 \langle E_{\nu_e} \rangle \langle E_{\bar{\nu}_e} \rangle} \int_0^\infty \int_0^\infty EE' (E + E') f_{\nu_e}(E) P_{\nu_e}(E, r) f_{\bar{\nu}_e}(E') P_{\bar{\nu}_e}(E', r) dE dE', \quad (\text{A12})$$

where $\Psi(r) = [D(r)]^4 \{[D(r)]^2 - 6D(r) + 10\}$, $\Lambda_{\nu_e \bar{\nu}_e} = C_V^2 + C_A^2$. In adapting the above rate to give $\dot{q}_{\nu_x \bar{\nu}_x}$, note that $\Lambda_{\nu_x \bar{\nu}_x} = (C_V - 1)^2 + (C_A - 1)^2$. The rate $\dot{q}_{e^- e^+}$ is

$$\dot{q}_{e^- e^+} = (\Lambda_{\nu_e \bar{\nu}_e} + 2\Lambda_{\nu_x \bar{\nu}_x}) \frac{2G_F^2 T^9}{9\pi^5 \rho} \left[g_{1,0,0} \left(\frac{m_e}{T}, \eta, 0, 0 \right) g_{2,0,0} \left(\frac{m_e}{T}, -\eta, 0, 0 \right) + g_{1,0,0} \left(\frac{m_e}{T}, -\eta, 0, 0 \right) g_{2,0,0} \left(\frac{m_e}{T}, \eta, 0, 0 \right) \right]. \quad (\text{A13})$$

REFERENCES

- Abazajian, K. N., Acero, M., Agarwalla, S., et al. 2012, arXiv preprint arXiv:1204.5379
- Bethe, H. A., & Wilson, J. R. 1985, *The Astrophysical Journal*, 295, 14
- Duncan, R. C., Shapiro, S. L., & Wasserman, I. 1986, *The Astrophysical Journal*, 309, 141
- Frohlich, C., Martinez-Pinedo, G., Liebendorfer, M., et al. 2006, *Phys. Rev. Lett.*, 96, 142502

- Fuller, G. M., Mayle, R. W., Wilson, J. R., & Schramm, D. N. 1987, *The Astrophysical Journal*, 322, 795
- Hoffman, R., Woosley, S., & Qian, Y.-Z. 1997, *The Astrophysical Journal*, 482, 951
- Janka, H.-T. 2012, *Annual Review of Nuclear and Particle Science*, 62, 407
- Malkus, A., McLaughlin, G., & Surman, R. 2016, *Physical Review D*, 93, 045021
- Martínez-Pinedo, G., Fischer, T., & Huther, L. 2014, *Journal of Physics G: Nuclear and Particle Physics*, 41, 044008
- McLaughlin, G., Fetter, J., Balantekin, A., & Fuller, G. 1999, *Physical Review C*, 59, 2873
- Meyer, B., Mathews, G., Howard, W., Woosley, S., & Hoffman, R. 1992, *The Astrophysical Journal*, 399, 656
- Mikheev, S., & Smirnov, A. Y. 1985, *Sov. J. Nucl. Phys.(Engl. Transl.);(United States)*, 42
- Nunokawa, H., Peltoniemi, J. T., Rossi, A., & Valle, J. 1997, *Physical Review D*, 56, 1704
- Pllumbi, E., Tamborra, I., Wanajo, S., Janka, H.-T., & Hüdepohl, L. 2015, *The Astrophysical Journal*, 808, 188
- Qian, Y.-Z., Fuller, G. M., Mathews, G. J., et al. 1993, *Physical review letters*, 71, 1965
- Qian, Y.-Z., & Woosley, S. 1996, *The Astrophysical Journal*, 471, 331
- Roberts, L., Woosley, S., & Hoffman, R. 2010, *The Astrophysical Journal*, 722, 954
- Sigl, G., & Raffelt, G. 1993, *Nuclear Physics B*, 406, 423
- Takahashi, K., Witt, J., & Janka, H.-T. 1994, *Astronomy and Astrophysics*, 286, 857
- Tamborra, I., Raffelt, G. G., Hüdepohl, L., & Janka, H.-T. 2012, *Journal of Cosmology and Astroparticle Physics*, 2012, 013
- Thompson, T. A., Burrows, A., & Meyer, B. S. 2001, *The Astrophysical Journal*, 562, 887
- Timmes, F., & Arnett, D. 1999, *The Astrophysical Journal Supplement Series*, 125, 277
- Timmes, F. X., & Swesty, F. D. 2000, *The Astrophysical Journal Supplement Series*, 126, 501
- Wanajo, S. 2013, *The Astrophysical Journal Letters*, 770, L22
- Wanajo, S., Kajino, T., Mathews, G. J., & Otsuki, K. 2001, *The Astrophysical Journal*, 554, 578
- Witt, J., Janka, H.-T., & Takahashi, K. 1994, *Astronomy and Astrophysics*, 286, 841
- Wolfenstein, L. 1978, *Physical Review D*, 17, 2369
- Woosley, S., & Baron, E. 1992, *The Astrophysical Journal*, 391, 228
- Woosley, S., & Hoffman, R. D. 1992, *The Astrophysical Journal*, 395, 202
- Woosley, S., Wilson, J., Mathews, G., Hoffman, R., & Meyer, B. 1994, *The Astrophysical Journal*, 433, 229
- Wu, M.-R., Duan, H., & Qian, Y.-Z. 2016a, *Physics Letters B*, 752, 89
- Wu, M.-R., Fernández, R., Martínez-Pinedo, G., & Metzger, B. D. 2016b, *Mon. Not. Roy. Astron. Soc.*, 463, 2323
- Wu, M.-R., Fischer, T., Huther, L., Martínez-Pinedo, G., & Qian, Y.-Z. 2014, *Physical Review D*, 89, 061303